An Overview of Recent Results from the TCV Tokamak

T.P. Goodman 1), S.M. Ahmed 1), S. Alberti 1), Y. Andrèbe 1), C. Angioni 2), K. Appert 1), G. Arnoux 1), R. Behn 1), P. Blanchard 1), P. Bosshard 1), Y. Camenen 1), R. Chavan 1), S. Coda 1), I. Condrea 1), A. Degeling 1), B.P. Duval 1), P. Etienne 1), D. Fasel 1), A. Fasoli 1), J.-Y. Favez 1), I. Furno 3), M. Henderson 1), F. Hofmann 1), J.-P. Hogge 1), J. Horacek 1), P. Isoz 1), B. Joye 1), A. Karpushov 1), I. Klimanov 1), P. Lavanchy 1), J.B. Lister 1), X. Llobet 1), J.-C. Magnin 1), A. Manini 2), B. Marlétaz 1), P. Marmillod 1), Y. Martin 1), An. Martynov 1), J.-M. Mayor 1), J. Mlynar 1), J.-M. Moret 1), E. Nelson-Melby 1), P. Nikkola 1), P.J. Paris 1), A. Perez 1), Y. Peysson 4), R.A. Pitts 1), A. Pochelon 1), L. Porte 1), D. Raju 5), H. Reimerdes 6), O. Sauter 1), A. Scarabosio 1), E. Scavino 1), S.H. Seo 1), U. Siravo 1), A. Sushkov 7), G. Tonetti 1), M.Q. Tran 1), H. Weisen 1), M. Wischmeier 1), A. Zabolotsky 1), G. Zhuang 1)

1) Centre de Recherches en Physique des Plasmas, Association EURATOM - Confédération Suisse, Ecole Polytechnique Fédérale de Lausanne, CRPP - EPFL, CH-1015 Lausanne, Switzerland
2) Max-Planck-Institute für Plasmaphysik, Garching bei München, Germany
3) Los Alamos National Laboratory, USA
4) DRFC-CEA Cadarache, France
5) Institute for Plasma Research, Bhat, Gandhinagar-382 428, Gujarat, India
6) General Atomics, San Diego, USA
7) RRC Kurchatov, Moscow, Russia

e-mail contact of main author: Timothy.Goodman@epfl.ch

Abstract. The TCV tokamak (R=0.88 m, a < 0.24 m, B < 1.54 T) program is based on flexible plasma shaping and heating for studies of confinement, transport, control and power exhaust. Recent advances in fully-sustained off-axis electron cyclotron (EC) current drive (CD) scenarios have allowed the creation of plasmas with high bootstrap fraction, steady-state reversed central shear and an electron internal transport barrier. High elongation plasmas, $\kappa = 2.5$, are produced at low normalized current using far off-axis EC heating (ECH) and ECCD to broaden the current profile. Third harmonic heating is used to heat the plasma center where the second harmonic is in cut-off. Both second and third harmonic heating are used to heat H-mode plasmas, at the edge and center, respectively. The ELM frequency is decreased by the additional power but in separate experiments can be controlled by locking to an external perturbation current in the internal coils of TCV. Spatially resolved current profiles are measured at the inner and outer divertor targets by Langmuir probe arrays during ELMs. The strong, reasonably balanced currents are thought to be thermoelectric in origin.

1. Introduction

Stable plasmas in which all of the current was driven by electron cyclotron current drive (ECCD) were first obtained in TCV (Tokamak à Configuration Variable) in 1999 [1]. Subsequently, 2.0s plasmas of up to 210kA were fully sustained using the complete installation of six, 82.7 GHz, 0.5 MW, 2.0 s gyrotrons coupling to the second harmonic X-mode (X2) [2]. In an extension of earlier results [3, 4], two pairs of gyrotrons operated in succession produced stable, 100kA, 4s discharges.

It was shown that when ECCD was concentrated at the plasma center, the plasma pressure and current profiles which resulted were unstable to ideal MHD modes. The modes appeared as the current profile relaxed to the new shape determined by the ECCD source. When the power was increased using additional gyrotrons, it was necessary to broaden the deposition profile to

ensure stability. This deposition broadening resulted in a lower overall efficiency as more of the power was deposited in regions of lower temperature, higher trapping and therefore lower efficiency [1, 2].

All of the ECCD experiments benefit to a certain extent from relatively low density (at the absorption location) due to the associated increase in current drive efficiency; as long as absorption is still completed on one side of the cold resonance and far enough from the trapped-passing boundary. The cut-off density for X2 is just over $4 \cdot 10^{19} [m^{-3}]$. Thus, for the purposes of this paper, the operational space of TCV can be crudely divided into regions of low and high density; referring to the accessibility of the X2 heating system to the plasma center. There is a smooth transition from one to the other, however, since X2 can be used at the plasma edge where the density remains low enough to allow access to the resonance.

The recent completion of the third harmonic X-mode heating system (X3), consisting of three, 118GHz, 0.5MW, 2.0s gyrotrons, has allowed operation with centrally deposited ECH in the higher density regime for the first time on TCV. Ohmic ELMing H mode studies are now extended to additionally heated discharges. In this paper, sections 2-5 deal with the lower density regime and 6-7 with the higher density regime (both Ohmic and additionally heated plasmas).

2. Scenarios Externally Sustained by Off-axis ECCD

Fully sustained ECCD driven plasmas are created by injecting co-ECCD into the current flattop of an established Ohmic plasma. After 20ms, the transformer coil current, I_{OH}, is feedback controlled at a constant current thereby precluding an external source for the inductive electric field in the plasma. The current in the shaping coils are constant in all cases of interest. Under these conditions, the total ECCD driven current is easily measured. Following the method described in Ref. 4, the derived ECCD current I_{CD} is found by subtracting the bootstrap current I_{BS} from the total plasma current, I_p.

The fully sustained ECCD driven results have now been extended to plasmas which are fully sustained only by *off-axis* co-ECCD. The non-inductive current profiles are broadened by radial diffusion of the fast particles so that some central current is still present. The off-axis deposition creates enough bootstrap current to produce a q-profile with reversed shear in the center. With the addition of counter-ECCD in the center, steep, wide, electron internal transport barriers (eITBs) are created with a subsequent increase in the bootstrap fraction to >50% [5]. The current profile is only determined by the gyrotron beam aiming, which defines the current drive and bootstrap current drive which is itself determined by the pressure profile resulting from the deposition profile and the shear dependent transport. We have obtained stable discharges lasting longer than $500\tau_E$ and 10 current diffusion times which have positive additional-power scaling for the central counter-ECCD. In general, TCV plasmas follow Rebut-Lallia-Watkins (RLW) scaling [6, 7] and we report confinement improvements relative to this value H_{RLW} [8, 9]. For these ITBs, $H_{RLW} = 4$ which is ~ 1.6 times ITER L-mode scaling. The following three subsections deal with the three important features of this scenario: *1)* radial diffusion of fast particles and the ECCD current profile, *2)* the bootstrap current, total current and resulting safety factor profiles, and *3)* the improved confinement of the eITB.

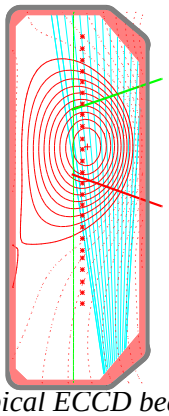

*FIG. 1. Typical ECCD beam aiming for off-axis ECCD (red, green lines), Thomson scattering measurement points (red *) and Hard X-ray camera chords (cyan lines).*

2.1. Current-Carrying Fast-Electron Diffusion

2.1.1. Direct Evidence of Fast-Electron Diffusion

An energy-resolved, multi-chord, Hard X-ray pinhole camera [10], on loan from CEA-Cadarache, is installed on the bottom of TCV. The 14 viewing chords pass vertically through the outer half of the plasma (FIG. 1). The measured photon temperature is nearly constant across the poloidal section, whereas the Abel-inverted emissivity peaks in the center (FIG. 2). Thus, direct evidence [11] for radial diffusion of fast electrons is provided by the hard X-ray camera as the beams do not pass through the plasma center and therefore cannot directly generate the fast population at that location. Measurements from the high field side, 24-channel, electron cyclotron emission (ECE) radiometer, operating in the 78-114 GHz range, are also sensitive to the fast electron population and, in conjunction with the hard X-ray results, are consistent with a suprathermal electron density of up to 25% of the total electron density [12]; derived using a bi-maxwellian temperature model.

2.1.2. Calculating the driven current

The magnitude of the driven current determined by linear calculations (e.g. TORAY-GA [13] or CQL3D [14] at artificially low power) is generally one to three times smaller than the measured (see below) driven current. Previous calculations of the current drive using the TORAY-GA ray-tracing code coupled to the quasi-linear Fokker-Planck code CQL3D, overestimated the driven current by an order of magnitude.

Diffusion and density conserving advection of the current-carrying fast electrons in physical space has been included in CQL3D with the diffusion coefficient as a free parameter [15], constrained by the experimental ECCD current, discussed above. Several models for the dependence of the diffusion on velocity have been studied: $D \propto v^{\alpha}$ with α = -1,0,1 [16]. The details of the resulting electron velocity distribution function are different in each case. However, the particles which carry the largest part of the current generally have a velocity ~ 5-6$v_{thermal}$ and for these particles, the diffusion coefficients are within a factor of three of each other for all of the models – typically 3-5 m^2/s [5]. Hard X-ray measurements place a lower bound of 1.5 m^2/s on D [11].

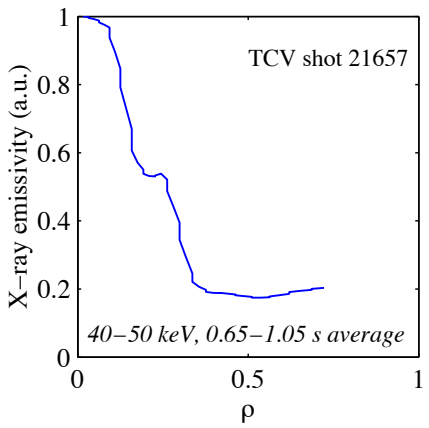

FIG. 2. Time-averaged, Abel inverted hard X-ray emission profile during 1 MW of off-axis co-ECCD; showing central emission at photon energies >40keV (T_e bulk ~ 2.7keV).

The most important consequence of diffusion is that the ECCD current profiles j_{CD} are typically flattened (or slightly hollow) towards the axis in contrast to the power deposition which is peaked off-axis. The total driven current is then, by choice of the free parameter, consistent with the measured plasma current after accounting for the bootstrap current.

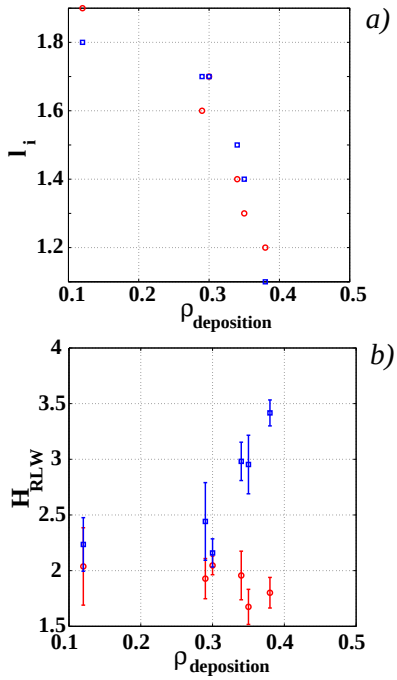

FIG. 3. a) Internal inductance decreases and b) H_{RLW} increases as the co-ECCD deposition is moved further off axis. Red points are before the addition of central counter-ECCD; blue points, after.

2.2. Importance of the Bootstrap Current

The electron temperature and density are measured by Thomson scattering at 25 points along a vertical chord in the TCV vessel (FIG. 1) every 50ms, for these discharges. The bootstrap current is calculated from the T_e and n_e profiles assuming steady state conditions [4]. The justification for this assumption is the observation that the reconstructed equilibrium parameters (e.g. internal inductance l_i and elongation κ) no longer evolve in time after a few 100ms.

During the first few 100ms of the ECCD, the power deposition is only off-axis, the density and temperature profiles tend to be flat in the plasma center, and the bootstrap current profile j_{BS} is peaked off-axis – amounting to ~20-25% of the total current. The combination of the flattened j_{CD} and j_{BS} leads to a hollow total current profile j_{TOT}. The calculated current profile and measured pressure profile is then input to the CHEASE equilibrium code to calculate the steady-state q-profile.

If the ECCD deposition is moved further off-axis, the steady-state internal inductance is reduced (FIG. 3a) and the pressure profile broadened. For deposition $\rho \equiv \sqrt{V_\psi / V_a} \approx 0.3$, where V_ψ is the volume inside a given flux surface and V_a the plasma volume, the plasmas begin to show evidence of improved confinement (H_{RLW} ~ 3.5) when power from an additional gyrotron is later added near the center (FIG. 3b). As the j_{CD} profiles are not peaked off-axis, this result shows that it is the bootstrap current that plays the key role in the ITB formation.

2.3. Steady State Electron Internal Transport Barrier

It has been shown [17, 18] that there is a gradual improvement in the H_{RLW} for these plasmas as small amounts of counter-ECCD are added near the center in order to increase the safety factor on axis. Excessive counter-ECCD leads to a disruption but, by adjusting the central launch angle, the plasma can be maintained just below the MHD stability limit. Figures 4a,b show the j_{CD}, j_{BS} and j_{TOT} profiles before (dashed curves) and after (solid curves) addition of counter-ECCD in the center and the resulting q-profile (after). The bootstrap current fraction is ~50% in this steady state discharge lasting ~$200\tau_{Ee}$ with ~ 1.6 times ITER L-mode scaling. At

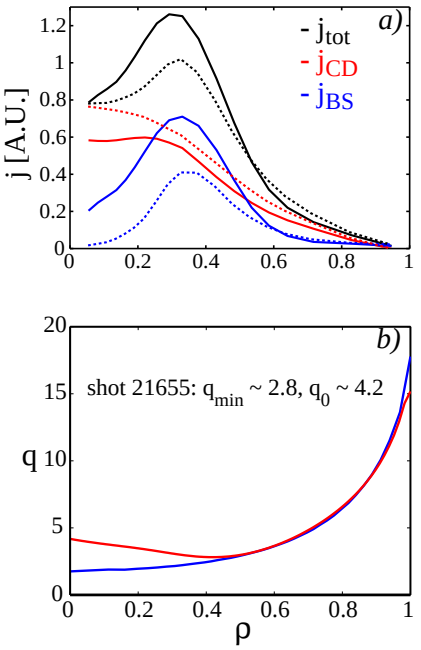

FIG. 4. a) CQL3D calculated j_{CD}, j_{BS} and j_{TOT} before (dashed) and after (solid) additional central counter-ECCD. b) The q-profile calculated by LIUQE (blue) and CHEASE (red).

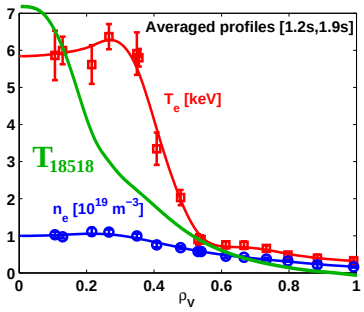

FIG. 5. Temperature profile in the ICEC (green - scaled with power) to the fully sustained, off-axis ECCD with central counter ECCD (red).

present, electron-ion coupling is low and T_e/T_i ~ 20 [19,18]. When the density is increased for this scenario, the current drive efficiency decreases but the bootstrap current, and especially the bootstrap fraction, increases [5].

3. The Improved Core Electron Confinement (ICEC) regime

In inductive discharges, stable regimes of improved core energy confinement were achieved ($H_{RLW} = \tau_E /(\tau_{E\ RLW})$ ~3.5) with and without sawteeth [8, 9] by a combination of off-axis ECH followed by central counter ECCD. PRETOR–ST, a1–1/2D transport code including a sawtooth crash model [20, 21], accurately simulates the measured electron temperature profiles in these discharges and indicates that the central shear is reversed [9]. The code successfully predicted that a 10% displacement of the central counter-ECCD would lead to a loss of the reversed shear and high confinement regime [3, 4]. This regime has narrower good confinement regions due to the natural peaking of the profiles caused by the residual electric field. Figure 5 shows a comparison between the ICEC regime and the off-axis driven ITBs described in section 2, above. In the ITB case, the temperature profile is wider and the foot of the barrier (where the temperature begins to deviate after the addition of the central counter-ECCD) is at larger ρ [18]. This results in a larger plasma volume in which the confinement is improved as well as the larger bootstrap fractions discussed above. Although most recent work has been carried out on the off-axis ITBs, a comparison of the two regimes should allow subtleties of non-maxwellian, hot conductivity induced enhancement of the current drive efficiency [22] to be addressed [4]. In addition, the ICEC regime yields better τ_{Ee} as I_p and n_e are larger.

4. Understanding the Control of The Sawtooth Instability

In sawtooth control experiments, 1.3MW of EC power deposited outside the q=1 produces sawtooth stabilization. To find the optimum location for stabilization, 3 gyrotron beams are swept across the region of the q=1 surface and the maximum sawtooth period is found. This technique is used to align each of the 6 independent EC launchers relative to each other to within ±3mm i.e. ~1% of the minor radius [23].The addition of 0.45MW of EC power deposited at an optimum location just inside q=1 then destabilizes the sawteeth [21]. This demonstrates that ECH may be able to destabilize the long-period sawteeth predicted in burning plasmas.

The sawtooth period and optimum locations for stabilization and destabilization are simulated successfully [21,24] with PRETOR-ST. In experiments, current drive is always accompanied by heating. The effects of heating and current drive can be separated in the simulations which is especially useful for understanding counter-ECCD where competing effects are at play [21]. The methodology used to find both the maximum or minimum in sawtooth period is the same in the code and in the experiments: the beams are swept in order to find the optimum location.

The sawtooth model is successful in showing that the optimum for stabilization is clearly outside the q=1 surface, in agreement with the experiments, and that the minimum is inside (for the conditions of the experiment see Ref. 21). The accuracy of the simulation appears quite high; the difference between the simulated and measured sawtooth period maximum is 3% in

ρ. Nevertheless, this difference is significant given the ~1% precision in launcher alignment. The accuracy of the results depends directly on the proper knowledge of the geometry of the launchers, plasma position and on the ray-tracing. The estimated accuracy in the geometry is of the same order as the simulations. The consequence is that it is not yet possible to *predict* the fixed launching angles of the beams that would be necessary to ensure optimum stabilization of the sawteeth: sweeps are a necessity. On the other hand, the optimum for destabilization is significantly broader in ρ and may not be as difficult to predict.

An alternative methodology (similar to [4]) could be applied by assuming that the modeling has the highest accuracy then, re-calibrating the launching geometry accordingly. It would still be necessary to determine whether the launchers or the magnetic reconstruction are in error.

5. The Link between Classical and Neoclassical Tearing Modes [25]

The theoretical dependence of Δ' on island width has been confirmed in experiments in which strong central ECCD modified the Ohmic current profiles of low density discharges, leading to a tearing mode with two distinct growth phases. The tearing mode appears on a current diffusion time scale and is driven unstable by the current profile. After growing to a sufficient width, it exceeds the critical island width for rapid growth of the neoclassical tearing mode. When the ECCD is switched off the island width decreases, first on a confinement and then a resistive diffusion time scale. These results unify the theory of classical and neoclassical tearing modes and therefore, the island width evolution is well modeled using the modified Rutherford equation.

6. Type-III ELMy H-modes on TCV

With additional heating on TCV, it has been shown that the ELM frequency decreases with increasing power. This is typically taken as one of the characteristic differences between type-III and type-I ELMs [e.g. 26]. Therefore the ELMs discussed below are referred to as type-III ELMs.

The transition from L-mode to ELM-free or type-III ELMy Ohmic H-mode has been studied statistically using the 'mobile centers method'. Ranges of plasma current, density, elongation, triangularity and plasma-wall distance have been determined in which it is possible to pass reliably into the ELMy H-mode. Once the ELMy H-mode is entered through this 'gateway', the plasma parameters can be varied within a significantly wider range while maintaining the ELMs. [27]

Unstable periodic orbits (UPO) in the ELM time series have been observed showing that a deterministic, chaotic process governs the apparently random distribution of the delay between ELMs on TCV [28]. These results imply that any valid theoretical model for type-III ELMs must account for the existence of UPOs. Statistical analysis of ELM and sawtooth periods indicates frequent synchronization of the ELM to half, equal, double or triple the sawtooth frequency, depending on the elongation [29].

6.1. Divertor Target Currents During Type-III ELMs

Arrays of single Langmuir probes embedded in central column and floor graphite protection tiles and biased at zero voltage provide high spatial and temporal resolution of currents that flow to the inner and outer divertor targets during ELMing phases of single null lower (SNL)

Ohmic H-modes. Many of these discharges are characterized by long phases of extremely regular Type III ELMs, permitting a coherently averaged ELM current to be generated at each probe using the peak of the signal of a vertical viewing D_α chord at each ELM to define the zero time reference. Careful choice of the averaging period (~ 4ms for a 200Hz ELM frequency) around each ELM ensures that each is unaffected by the preceding or following event. Standard TCV operation uses positive plasma current and toroidal field, with the latter defining the ion ∇B drift direction away from the X-point for SNL equilibria. The coherent ELMs in FIG.s 6a-c show that near the strike points, large negative and positive currents flow to the inner and outer targets respectively, with the currents reaching peak values at the peak of the D_α recycling signal intensity. These currents are comparable in magnitude to the ion saturation current - the maximum current that can flow to the grounded tiles.

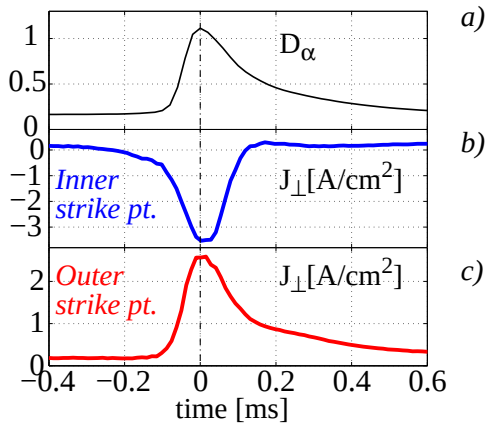

FIG. 6. Coherently averaged ELMs for D_α (a) used as the reference timing trace and perpendicular target current near the strike point at the inner (b) and outer (c) targets.

Figure 7 shows a selection of perpendicular target current profiles mapped to the outside midplane of the equilibrium and plotted as a function of distance from the separatrix for a selection of time intervals before, during and after the coherent ELM. Reasonable current balance is obtained during the ELM itself across most of the profile. The persistent, localized and unbalanced negative current feature appearing very close to the strike point at the inner target before and after the ELM is of the expected sign for a parallel current driven by the effects of the ∇B drift and the up-down asymmetry of plasma pressure. During the ELM, the broad parallel current profile is believed to be thermoelectric in origin. In L-mode, at the relatively low plasma densities common to the H-mode ELMing phase studied here, the unfavorable ∇B drift direction leads to strong in/out asymmetries in the divertor plasma parameters, with the inner target generally hotter than the outer. Though fast T_e measurements cannot be made during the ELM event itself, if the hot electrons expelled by the ELM were to accentuate the in/out T_e asymmetry, an electron thermocurrent would be expected to flow from the colder outer target to the hotter inner target. The experimental currents in FIG.s 6,7 do indeed flow in this direction. Integrating the profiles radially and toroidally yields total perpendicular target currents ~2-3 kA – of the order of 0.7% of the plasma current.

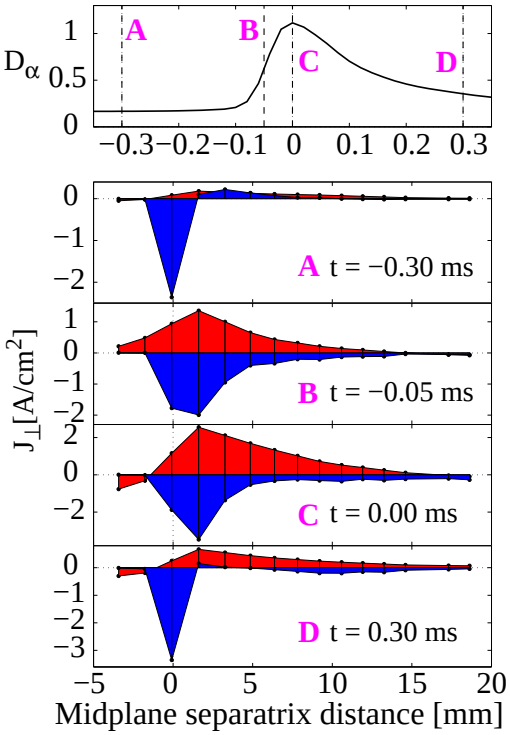

FIG. 7. Profiles of perpendicular target currents mapped to the outside magnetic midplane at various times during the coherent ELM (marked as A-D on the coherent D_α trace at top). Strong and reasonably balanced currents flow at all locations during the ELM.

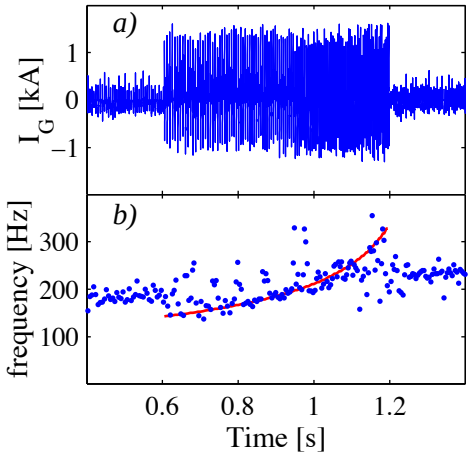

FIG. 8. a) Perturbation creating vertical motion (~±3mm) to the feedback controlled vertical stability coil current I_G. b) Frequency tracking of the ELMs (blue dots) to the drive frequency (red line).

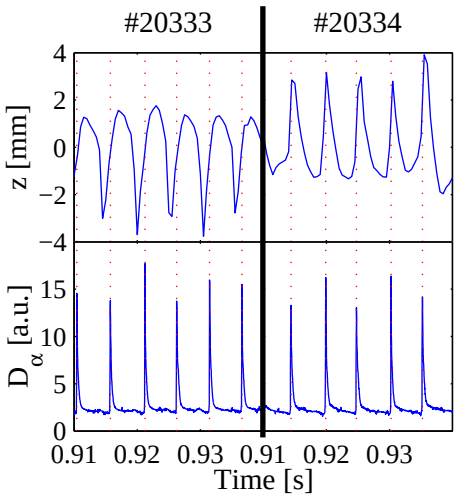

FIG. 9. Triggering of the ELM (lower traces) by the upward vertical motion (upper traces) for two shots with opposite polarity of the driving perturbation.

6.2. ELM Frequency Controlled by Vertical Plasma Motion

The ELM frequency has been experimentally locked to a modulation of the fast coil current inside the TCV vessel which was swept in frequency [30]. A 2 ms, single-cycle, square-wave voltage perturbation is used to drive a current in the internal fast coils. The resulting current pulse is roughly triangular and is added to the regular feedback control loop used to stabilize the vertical position. The additional perturbation induces a vertical motion of the plasma up to ±2-3mm. The pulses are repeated at a swept frequency close to the natural ELM frequency of approximately 200Hz. When the amplitude is small, the phasing between the perturbation and the ELMs scrolls continuously as the frequency is swept from 143 Hz to 333 Hz over 0.6 seconds. Increasing the amplitude of the perturbation causes the ELM frequency to track the frequency of the vertical perturbations. Figure 8 shows that the ELM frequency can be both reduced or, more importantly, increased. It is also observed that during tracking, ELMs are triggered on the upward vertical motion independent of the polarity of the voltage pulses which are used to cause the perturbation. That is, if the phase of the single cycle square wave is shifted by 180°, the ELMs still occur when the plasma is moving upwards (FIG. 9). The asymmetry in the poloidal field for lower single-null diverted plasmas is such that an upward vertical motion corresponds to an induced current at the edge in the same direction as the plasma current.

6.3. ELM Frequency Modification with Additional Heating

6.3.1. Edge Heating with X2

ELMing Ohmic H-mode plasmas with central density of $n_{e0} = 1.5 \cdot 10^{20} m^{-3}$ have been heated using X2. The density cutoff of the X2 is reached near the edge of the plasma ($\rho > 0.9$) and the refraction is very strong. The heat is localized at the plasma edge and amounts to only ~40% of the beam power – the rest being absorbed or lost after multiply reflections from the inner wall of the vacuum chamber. The X2 power pulses were, therefore, kept short. The ELM frequency decrease from 200 ±40 Hz without ECH, to 140±40Hz with 0.45 MW of injected

power. Because of the large refraction this scenario is technically undesirable.

6.3.2. Central Heating with X3 [31]

A 3-gyrotron, 1.5MW, 118GHz, 2.0s third harmonic electron cyclotron resonance heating system (X3) has been installed, commissioned and brought into operation on TCV [32]. It has been used to heat plasmas at densities up to $10^{20}m^{-3}$, far exceeding the cut–off density of the X2 system. The X3 system therefore significantly extends the operational parameter space of TCV and allows additionally heated H-mode plasmas to be studied [33].

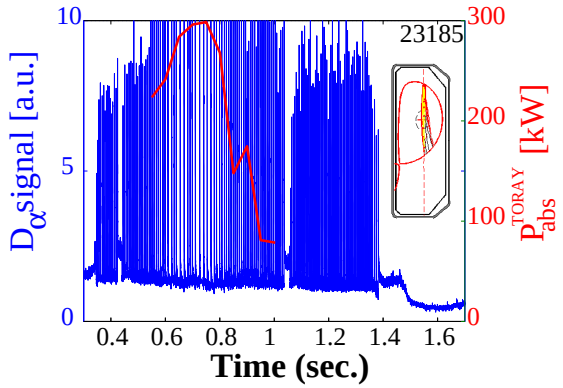

FIG. 10. The ELM frequency of the D_a signal (blue) is seen to decrease when the X3 power (red) is well absorbed during a mirror sweep. The inset shows the central ray of the beam at different times during the mirror sweep.

The X3 power is launched into TCV from the top and takes advantage of the longer path length along the resonance, especially at high κ, to compensate for the low optical depth at the third harmonic frequency. In fact, in the presence of the non-maxwellian electron distribution functions generated by X2 ECCD, it has been shown that 100% absorption can be obtained even when launching from the LFS [34]. The disadvantage of launching from the top is that the absorption is very sensitive to the injection angle and refraction. Feedback will be required to maintain the optimum heating angle. On the other hand, the launching mirror can be offset in major radius to allow incidence on the resonance from either the high or low field side. This feature should allow selective absorption on different energy regions in the electron distribution function.

ELMy H-mode plasmas with central density of $n_{e0} = 0.7 \cdot 10^{20}m^{-3}$ have been heated using up to 0.85MW (2 gyrotrons) of X3 power. Figure 10 shows the D_α time trace and the absorption of power from one X3 gyrotron, calculated by the TORAY-GA ray-tracing code, during a sweep of the launching mirror. The ELM frequency is seen to decrease as more power is absorbed and then increase again as the absorption drops due to non-optimum aiming. At the optimum angle, the absorption reaches 70%. When 0.85MW is injected at the optimum launcher angle, the ELM frequency decreases, an ELM free period ensues, a more global instability occurs which reaches the plasma center and the plasma returns to L-mode before terminating in a disruption. This can be prevented using the natural tendency of the ELM frequency to increase with decreasing density to counteract the frequency decrease with increasing power. A pre-programmed density decrease maintains the ELMy H-mode throughout the ECH pulse.

7. Extended High-κ Scenarios with ECH/ECCD

Advances have been made using both the X2 and X3 current drive / heating systems in highly shaped discharges. The aim of these experiments is to explore the region of β, I_N parameter space ($I_N = I \cdot a/B$ where I is the plasma current, a is the minor radius and B is the toroidal field) in which the so-called beta limit and current limits meet at high elongation [35]. By increasing the elongation, the current can be increased and I_N increases. The so-called current limit (q=2) is modified with elongation in such a way that it is necessary to reduce the current to obtain the

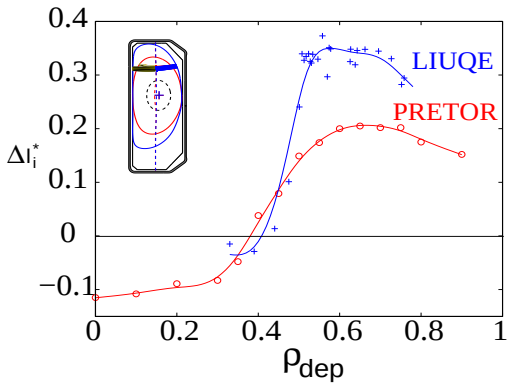

FIG. 11. Measured (blue) and calculated (red) change in the internal inductance due to ECH induced profile broadening. The inset shows two time slices of a typical shot with κ increasing due to far off axis ECH (colors are aribitrary).

highest possible beta. With Ohmic heating only the current limit has been reached [36] at low q and high κ, but it is not possible to reach the highest β–limit without additional heating. In high elongation discharges, the theoretical β-limit reaches a maximum at $I_N \sim 2$MA/mT. Thus, high elongation operation is required at lower plasma currents. This renders the high elongation plasma more vertically unstable. Current broadening with far off-axis X2 ECH/ECCD improves the stability at high κ and lower normalized current I_N.

7.1. Far Off-axis X2 heating and current drive

Plasma operation with $I_N \sim 2$MA/mT imposes technical limits on X2 accessibility in TCV due to high density and subsequent strong refraction of the beams; especially those launched near the plasma equator (2 beams) [37]. On the other hand, for efficient elongation of the plasma by current profile broadening with far-off axis X2, it is desirable to increase the density thereby maintaining high X2 absorption even when depositing nearer the plasma edge. The equatorial beams are then not usable due to refraction.

At present, highly elongated plasmas ($\kappa \sim 2.5$) with a high safety factor ($q_{edge} \sim 12$) and lower current ($I_p \sim 390$ kA, $I_N = I_p/aB = 1.03$ MA/mT) have been created using 1.35MW of far off-axis ECH [38] from 3 upper lateral launchers. The most efficient X2 heating location for current profile broadening has been determined [38] as shown in FIG. 11.

The magnitude of the change in internal inductance Δl_i^* achieved when far off-axis X2 heating is added to an Ohmic plasma (relative to the change in l_i that would be expected for the equivalent κ without heating) is plotted as a function of the deposition location, ρ_{dep} (blue curve: LIUQE). Positive Δl_i^* indicates an increase in κ with additional heating and negative Δl_i^*, a decrease. The plasma current is kept constant by feedback control and the shaping fields are also constant: the change in elongation is a result of the ECH generated profile broadening. The PRETOR transport code and DINA free-boundary evolution code calculations [39] (using the ECH heating profiles determined by TORAY-GA as additional input) show good agreement with the experiments. Both curves roll over when deposition is too far off axis. This is thought to be due to the increasingly poor confinement at large ρ. Adding either co- or counter-ECCD helps increase the efficiency of elongation [38]. The symmetry of this situation is under investigation but may be due to strong trapping effects (accentuated at large ρ). The operational space can be increased towards higher β by combining far off-axis X2 heating with central X3 heating.

7.2. Central Heating with X3

As in H-mode plasmas, the X3 system is essential for central heating of high density plasmas. The high κ increases the absorption depth yielding reasonable first pass absorption. The deposition profile is nevertheless broad. When central X3 is added to the plasmas elongated by far

off-axis X2 the current profile peaks as the central conductivity increases. By introducing an ECCD component to the X2 beams, suprathermal electrons are created which enhance the absorption of X3 [40] in a way similar to the earlier LFS X3 experiments [21]. As in the case of fully ECCD plasmas, the difference between Thomson scattering temperatures and ECE temperatures, as well as the localization of the emission during X3 modulation, indicates direct absorption of the X3 on the suprathermal population [40]. Up to 100% X3 absorption has been measured during top-launched, modulated X3 ECH experiments using the diamagnetic loop to measure the accompanying modulation of the stored plasma energy as in [21].

Before further advancing towards the β-limit, it is necessary to optimize the X3 heating scenario to avoid current peaking. To this end feed forward elongation control is used to help maintain the broadened profile when X3 is added [40].

8. Outlook

The development of fully sustained, steady state, eITB operation at high bootstrap fraction opens the way to full sustainment of the current using 100% bootstrap fraction. Investigation and control of ELMing H mode plasmas with electron heating can now be persued using the 1.5MW X3 heating system. The flexible, dual frequency, heating system of TCV can selectively excite different portions of the electron velocity distribution providing an ideal testbed for the study of ECCD physics, fast particle diffusion, thermal transport modelling and MHD instability control.

Acknowledgement: This work is partly supported by the Swiss National Science Foundation.

9. References

[1] SAUTER, O., et al., Proc. of the 26th EPS Conf. on Plasma Phys. and Control. Fusion, Maastricht, 1999, [ECA **23J** (1999) 1105], http://epsppd.epfl.ch/Maas/web/pdf/p3041.pdf; SAUTER, O., et al., Phys. Rev. Lett. **84** (2000) 3322.
[2] CODA, S., et al., Plasma Phys. Control Fusion **42** (2000) B311.
[3] GOODMAN, T.P., TCV Team, in Fusion Energy 2000 in (Proc. 18th Int. Conf. Sorrento, 2000), IAEA, Vienna (2001) CD-ROM file EXP4/09 and http://www.iaea.org/programmes/ripc/physics/fec2000/html/node1.htm.
[4] SAUTER, O., et al., Phys. Plasmas **8** (2001) 2199.
[5] GOODMAN, T.P., et al., in Proc. of the 29th EPS Conf. on Plasma Phys. and Control. Fusion, Montreux, 2002, [ECA **26B** (2002) P-2.081].
[6] REBUT, P.H., et al., Proc. 12th IAEA Conf., Nice 1988, IAEA, Vienna, **12** (1989) 191.
[7] WEISEN, H., et al., Nucl. Fusion **37** (1997) 1741.
[8] PIETRZYK, Z.A., et al., Phys. Plasmas **7**(2000) 2909.
[9] PIETRZYK, Z.A., et al., Phys. Rev. Lett. **86** 1530 (2001) 1530.
[10] PEYSSON, Y., CODA, S., IMBEAUX, F., Nucl. Instrum. and Methods in Phys. Res. A **458** (2001) 269.
[11] CODA, S., et al., in Proc. of the 29th EPS Conf. on Plasma Phys. and Control. Fus., Montreux, 2002, [ECA **26B** (2002) 0-4.03]; CODA, S., et al. Proc. of the 26th EPS Conf. on Control. Fusion and Plasma Phys., Maastricht, 1999, [ECA **23J** (1999) 1097].
[12] BLANCHARD, P., et al, Plasma Phys. Control. Fusion **44** (2002) 2231.
[13] MATSUDA, K., IEEE Trans. Plasma Sci. PS-17 (1989) 6.
[14] HARVEY, R.W., et al., Proc. of the IAEA Tech. Conf. on Advances in Simulation and Models of Thermonuclear Plasmas, Montreal, 1992, (IAEA, Vienna, 1992).

[15] HARVEY, R.W., SAUTER, O., PRATER, R. and NIKKOLA, P., Phys. Rev. Lett. **88** (2002) 205001.
[16] NIKKOLA, P., et al., to be published in Theory of Fusion Plasmas (Proc. Joint Varenna-Lausanne Int. Workshop) (Varenna 2002), edited by J.W. Connor, O. Sauter and E. Sindoni, ISPP-20 (Bologna, Editrice Compositori) (2002); NIKKOLA, P., et al., in Proceedings of the 12th Joint Workshop on ECE and ECRH, Aix-en-Provence, May 13-16, 2002 (World Scientific, Singapore, 2002) 257.
[17] SAUTER, O., et al., in Proc. of the 29th EPS Conf. on Plasma Phys. and Control. Fusion, Montreux, 2002, [ECA **26B** (2002) P-2.087].
[18] SAUTER, O., et al., this conference EX/P5-06.
[19] BOSSHARD, P., et al., Proc. of the 28th EPS Conf. on Control. Fus. and Plasma Phys., Madeira, 2001, edited by C. Silva, C. Varandas and D. Campbell [ECA **25A** (2001) 365].
[20] PORCELLI, F., BOUCHER, D., and ROSENBLUTH, M.N., Plasma Phys. Control. Fusion **38** (1996) 2163.
[21] ANGIONI, C., et al., submitted to Nucl. Fusion; ANGIONI, C., et al., in Proc. of the 29th EPS Conf. on Plasma Phys. and Control. Fusion, Montreux, 2002, [ECA **26B** (2002) P-1.118].
[22] FISCH, N.J., Phys. Fluids **28** (1985) 245.
[23] HENDERSON, M.A., et al., Fusion Eng. Des. **53** (2001) 241.
[24] GOODMAN, T.P., et al., this conference EX/P5-11.
[25] REIMERDES, H., SAUTER, O., GOODMAN, T.P., POCHELON, A., Phys. Rev. Lett. 88 (2002) 105005-1; REIMERDES, H., PhD Thesis, Lausanne Internal Report LRP 700/01 (2001).
[26] SUTTROP, W., Plasma Phys. Control. Fusion **42** (2000) A1
[27] MARTIN, Y., TCV Team, in Fusion Energy 2000 (Proc. 18th Int. Conf. Sorrento, 2000), IAEA, Vienna (2001) CD-ROM file EXP5/30 and http://www.iaea.org/programmes/ripc/physics/fec2000/html/node1.htm
[28] DEGELING, A.W., et al., Plasma Phys. Control. Fusion **43** (2001) 1671.
[29] MARTIN, Y.R., DEGELING, A.W., LISTER, J.B., Plasma Phys. Control. Fusion **44** (2002) A373.
[30] DEGELING, A.W., et al., in Proc. of the 29th EPS Conf. on Plasma Phys. and Control. Fusion, Montreux, 2002, [ECA **26B** (2002) P-2.078]
[31] PORTE, L., et al., this conference EX/P5-15.
[32] HOGGE, J-Ph., et al., in Proceedings of the 12th Joint Workshop on ECE and ECRH, Aix-en-Provence, May 13-16, 2002 (World Scientific, Singapore, 2002) 371.
[33] ALBERTI, S., et al., in Proc. of the 29th EPS Conf. on Plasma Phys. and Control. Fusion, Montreux, 2002, [ECA **26B** (2002) P-2.073].
[34] MANINI, A., et al., Plasma Phys. Control. Fusion **44** (2002) 139; GOODMAN, T.P., et al., Proc. of the 28th EPS Conf. on Control. Fus. and Plasma Phys., Madeira, 2001, edited by C. Silva, C. Varandas and D. Campbell [ECA **25A** (2001) 925]; ALBERTI, S., et al., in Fusion Energy 2000 (Proc. 18th Int. Conf. Sorrento, 2000), IAEA, Vienna (2001) CD-ROM file PD/2 and http://www.iaea.org/programmes/ripc/physics/fec2000/html/node1.htm
[35] HOFMANN, F., et al., Phys. Rev. Lett. **81** (1998) 2918.
[36] HOFMANN F. et al., Plasma Phys. Control. Fusion **43** (2001) A161.
[37] POCHELON, A., et al., Nucl. Fusion **41** (2001) 1663.
[38] CAMENEN, Y., et al., in Proceedings of the 12th Joint Workshop on ECE and ECRH, Aix-en-Provence, May 13-16, 2002 (World Scientific, Singapore, 2002) 407.
[39] RAJU, D., et al., in Proc. of the 29th EPS Conf. on Plasma Phys. and Control. Fusion, Montreux, 2002, [ECA **26B** (2002) P-2.082].
[40] POCHELON, A., et al., this conference, EX/P5-14.